Submitted 8/6/07 JFC

Radiolytic Gas-Driven Cryovolcanism in the Outer Solar System

John F. Cooper[1], Paul D. Cooper[2], Edward C. Sittler[3], Steven J. Sturner[4,5], Abigail M. Rymer[6], and Matthew E. Hill[6]

[1]*Heliospheric Physics Laboratory, Code 672, NASA Goddard Space Flight Center, 8800 Greenbelt Road, Greenbelt, MD, 20771 USA*

[2]*Department of Chemistry and Biochemistry, MS 3E2, George Mason University, 4400 University Drive, Fairfax, VA, 22030 USA*

[3]*Geospace Physics Laboratory, Code 673, NASA Goddard Space Flight Center, Greenbelt, MD, 20771 USA*

[4]*CRESST and Astroparticle Physics Laboratory, Code 661, NASA Goddard Space Flight Center, Greenbelt, MD 20771, USA*

[5]*Universities Space Research Association, 10211 Wicopin Circle, Suite 500, Columbia, MD 21044, USA*

[6]*Applied Physics Laboratory, Johns Hopkins Laboratory, 11100 Johns Hopkins Road, Laurel, MD 20723-6005, USA*

submitted to Journal of Geophysical Research - Planets, August 6, 2007

Abstract

Water ices in surface crusts of Europa, Enceladus, Saturn's main rings, and Kuiper Belt Objects can become heavily oxidized from radiolytic chemical alteration of near-surface water ice by space environment irradiation. Oxidant accumulations and gas production are manifested in part through observed H_2O_2 on Europa. tentatively also on Enceladus, and found elsewhere in gaseous or condensed phases at moons and rings of Jupiter and Saturn. On subsequent chemical contact in sub-surface environments with significant concentrations of primordially abundant reductants such as NH_3 and CH_4, oxidants of radiolytic origin can react exothermically to power gas-driven cryovolcanism. The gas-piston effect enormously amplifies the mass flow output in the case of gas formation at basal thermal margins of incompressible fluid reservoirs. Surface irradiation, H_2O_2 production, NH_3 oxidation, and resultant heat, gas, and gas-driven mass flow rates are computed in the fluid reservoir case for selected bodies. At Enceladus the oxidant power inputs are comparable to limits on non-thermal kinetic power for the south polar plumes. Total heat output and plume gas abundance may be accounted for at Enceladus if plume activity is cyclic in high and low "Old Faithful" phases, so that oxidants can accumulate during low activity phases. Interior upwelling of primordially abundant NH_3 and CH_4 hydrates is assumed to resupply the reductant fuels. Much lower irradiation fluxes on Kuiper Belt Objects require correspondingly larger times for accumulation of oxidants to produce comparable resurfacing, but brightness and surface composition of some objects suggest that such activity may be ongoing.

Introduction

Explosive volcanism on Earth originates from gas-driven (mostly H_2O vapor and CO_2) ejection at high temperature of an incompressible fluid from a subsurface magma reservoir to the planetary surface. High temperatures and plume gas output from volcanic hot spots at Io suggest a similar propulsive process. Comet outgassing from solar heating on approach to the Sun is well known, presumably involving release of trapped gases from cometary ices. Outgassing of N_2 has previously been detected [*Soderblom et al.*, 1990] by Voyager 2 at Triton, the largest moon of Neptune, and appears to be similarly driven by solar heating [*Brown et al.*, 1990; *Kirk et al.*, 1990], but the presence of subsurface fluids is unknown. Charon now shows potential surface evidence in ammonia hydrates for cryovolcanic flows from the subsurface [*Cook et al.*, 2007]. Absence of any ongoing surface change on Europa [*Phillips et al.*, 2000] suggests lack in the surface-accessible ice crust environment of cryovolcanic energy sources. A thick ice crust would likely preclude direct access to Europa's surface of dissolved gases from a putative subsurface ocean indicated by surface geologic features and induced magnetic fields [*Pappalardo et al.*, 1999].

Dramatically visible ice plume activity at Enceladus [*Porco et al.*, 2006] now provides unique opportunities for investigation with repeated observations during the continuing Cassini mission at Saturn. The measured presence of H_2O, CH_4, simple hydrocarbons, and a yet-unresolved mixture of CO and N_2 [*Waite et al.*, 2006] in the plume gas may indicate cryovolcanism involving the liquid water reservoir inferred by *Porco et al.* [2006]. However, a comet-like process involving only heat-driven release of trapped gases from ice clathrates has also been suggested [*Kieffer et al.*, 2007]. Although NH_3 is not highly abundant in either the plume gas [*Waite et al.*, 2006] or in the surface ice [*Brown et al.*, 2006], high temperature chemistry at the deep core-mantle boundary has been proposed by *Matson et al.* [2006] as the gas and hydrocarbon source.

64 Here we propose an alternative process for production of volatile gases that could drive
65 cryovolcanism on Enceladus and other icy bodies with irradiated near-surface water ices.
66 This process arises from interaction of continuously produced radiolytic oxidants and
67 primordial chemistry. First, the unique aspect of this model is that chemical energy for
68 oxidation arises in the outer ice crusts of planetary bodies from the continuous irradiation of
69 near-surface water ice by energetic charged particles from the magnetospheric, heliospheric,
70 and local interstellar space environments. Second, chemical energy and cryovolcanic driver
71 gases are released by oxidation of primordially abundant reduced "fuel" compounds
72 including ammonia, methane, and other hydrocarbons that originally accreted with water ice
73 to form the underlying low density ice mantles of these bodies. Gravitational tides, internal
74 tectonic activity, and radioisotope decay provide internal heating to increase rates of oxidant-
75 fuel chemical reactions in cryogenic ice environments. The high exothermic energy yields of
76 these reactions can potentially make the reactions self-sustaining. The subsurface liquid
77 reservoir advocated for Enceladus by *Porco et al.* [2006] would provide an ideal high thermal
78 gradient environment around the ice-liquid margins of the reservoir to sustain such reactions.
79 Since reaction rates would increase with temperature in the 80 – 273 K range expected at the
80 margins of a high-temperature water reservoir, exothermic heat production would raise local
81 temperatures at reaction sites, and the reactants may concentrate in these locations, explosive
82 results might be expected as observed.

83 The primary oxidant, O_2, in Earth's atmosphere comes from biological photosynthesis, but
84 surface oxidants on icy surfaces in the outer solar system are naturally produced in exposed
85 water ice by radiolysis from irradiation by energetic charged particles and solar ultraviolet
86 photons. Europa, Ganymede, and Saturn's rings all have atmospheric environments of
87 molecular oxygen presumably arising from particle or photon irradiation [*Hall et al.*, 1995,
88 1998; *Johnson et al.*, 2006], while all three icy Galilean moons have condensed phase O_2 in
89 the surface ice [*Spencer et al.*, 1995; *Spencer and Calvin*, 2002]. Ozone is a sensitive proxy
90 for atmospheric oxygen and is detected at Ganymede [*Noll et al.*, 1996], as well as at the
91 Saturn moons Dione and Rhea [*Noll et al.*, 1997]. Presence of oxidants may be indirectly

92 indicated by detection of atmospheric CO_2 as a potential oxidation product at Callisto
93 [*Carlson*, 1999] and of surface CO_2 at Europa [*McCord et al.*, 1998b], Ganymede [*Hibbitts et*
94 *al.*, 2003], and Callisto [*Hibbitts et al.*, 2000, 2002]. Further Callisto spectral observations
95 and associated models [*Strobel et al.*, 2002; *Liang et al.*, 2005] suggest that atmospheric O_2,
96 CO_2, and CO may be even more abundant on Callisto than the CO_2 first reported by Carlson
97 [1999]. Cassini spectral mapping measurements [*Buratti et al.*, 2005] show CO_2 in the ice-
98 rich surface environment of the small outer moon Iapetus at Saturn. The present paper
99 explores the possibility that N_2 and CO_2 in the Enceladus plume gas [*Waite et al.*, 2005]
100 might arise as oxidation products of radiolytic processes.

101 The radiolytic oxidant of highest known yield, hydrogen peroxide (H_2O_2), is produced in
102 low-temperature laboratory measurements [*Johnson et al.*, 2004; *Moore and Hudson*, 2000;
103 *Gomis et al.*, 2004a, 2004b; *Loeffler et al.*, 2006a] at yields of G = 0.1 – 0.4 H_2O_2 molecules
104 per 100 eV of ionisation energy deposited by incident primary charged particles. The
105 measured yield depends on existing abundances of other oxidants and is highest in the
106 presence of O_2 and CO_2 within the irradiated ice. Although present experimental yields for
107 direct production of O_2 are highly uncertain [*Johnson et al.*, 2004] by orders of magnitude at
108 $G = 10^{-4}$ to 10^{-1}, even slow accumulation over millions of years in volume ice could saturate
109 the ice crusts of irradiated icy moons and ring bodies, while also boosting the H_2O_2 yield and
110 cumulative concentrations. Sublimation of directly irradiated water ice can also concentrate
111 the H_2O_2 product [*Loeffler et al.*, 2006a], potentially producing explosive [Andrews, 1990]
112 heating and oxidation transients upon exothermic dissociation of the concentrated peroxide.

113 Hydrogen peroxide has been detected at the maximally high source rates on Europa's
114 heavily irradiated surface with surface concentrations ~ 0.1% relative to water ice [*Carlson et*
115 *al.*, 1999] and is possibly present as a UV-absorbing component in surface ices of Ganymede
116 and Callisto [*Hendrix et al.*, 1999a, 1999b]. There are preliminary reports of detection via
117 near-infrared absorption on Enceladus [*Newman et al.*, 2006, 2007]. The relatively short
118 lifetimes (four days at Jupiter, twenty days at Saturn) for H_2O_2 dissociation by solar

ultraviolet photons make surface detection difficult at sensible depths up to a few hundred micrometers. Products of more penetrating irradiation at millimeter to meter depths [*Cooper et al.*, 2001] beyond the UV penetration range ~0.15 μm [*Carlson et al.*, 1999] would, however, continue to accumulate. Furthermore, burial of radiation products by water frost deposition from cryovolcanic emissions may be faster than the production rate. Burial by meteoritic impact gardening may also protect radiolytic products from photolytic destruction as suggested earlier for Europa [*Cooper et al.*, 2001].

Low abundances of gaseous CH_4 in the atmospheres of Earth, and of Mars [*Formisano et al.*, 2004; *Mumma et al.*, 2004], illustrate that oxidants and reductants cannot long co-exist in chemically reactive environments where continuous sources must replenish the observed gas. The presence of abundant frozen CH_4 on Pluto, Eris, and other Kuiper Belt Objects [*Cruikshank et al.*, 1997; *Brown et al.*, 2005], and of atmospheric CH_4 on Titan [*Niemann et al.*, 2005], indicates that oxidized water ices are not presently in direct chemical contact with the sensible surfaces and atmospheres of these bodies. However, the CH_4 surface layers on icy bodies, and the dominant CH_4 hydrocarbon in Titan's atmosphere, could be ejecta from past and even ongoing cryovolcanism, as arising from occasional interactions of otherwise segregated oxidant and reductant concentrations in the near-surface environment.

Fluid environments are thought to be essential for evolution of life but also enable the dramatic effects of gas-driven volcanism by the combined gas-piston interaction of subsurface fluids and gases. Liquid water oceans at tens to hundreds of kilometres in depth may account for induced magnetic field measurements at the icy Galilean moons of Jupiter [*Kivelson et al.*, 2004], and a south polar water reservoir may account in part for the plume activity at Enceladus. Other internal heat sources, e.g. radioisotope decay, may account for modern presence of fluids even in cases of weak tidal heating, as at Callisto [*McKinnon*, 2006; *McKinnon and Barr*, 2006]. If so, even the icy dwarf planets of the Kuiper Belt, many much larger than Enceladus, might have subsurface reservoirs of the requisite incompressible

145 fluids at eutectic temperatures, e.g. 173 K for H_2O-NH_3 mixtures, to enable active
146 cryovolcanism.

147 In this paper we quantitatively model radiolytic gas-driven cryovolcanism for illustrative
148 cases of Enceladus and elsewhere in terms of the proposed sequence of radiolytic chemical
149 processes from surface irradiation and oxidant production, to exothermic H_2O_2 dissociation
150 and fuel oxidation, and finally to gas production giving rise to plume emissions. Underlying
151 assumptions in the model are vertical mobility of radiolytic products and underlying fuel
152 compounds in the south polar ice crust, trace abundances of metal catalysts to trigger H_2O_2
153 dissociation even at low temperatures, an unlimited supply of fuel compounds presumably
154 brought up by rheological flows from deep primordial reservoirs, and a subsurface H_2O fluid
155 reservoir that underlies the polar cap. The fluid reservoir provides a steep thermal gradient
156 around its warm ice margins to accelerate exothermic chemical reactions, becomes
157 pressurized with gaseous oxidation products, and provides the bulk of plume mass flow
158 through gas-driven propulsion of the incompressible fluid. Using representative flux spectra
159 for electron or proton irradiation in selected orbital environments of the outer solar system,
160 we compute the radiolytic model parameters for icy bodies in these environments under the
161 above common assumptions to show the full potential range of cryovolcanism that could be
162 driven by radiolytic gases in diverse outer planet environments from Europa and Enceladus to
163 the Kuiper Belt and the Oort Cloud. In the final discussion we then characterize the strengths
164 and weaknesses of this model with respect to those of other models previously published and
165 widely reported for Enceladus.

166 **Enceladus**

167 The water ice [*Porco et al.*, 2006], neutral gas [*Waite et al.*, 2006], and dust [*Spahn et al.*,
168 2006] plumes of Enceladus provide the second known example of active cryovolcanism and
169 are also produced, like on Triton, in an icy surface heavily irradiated by energetic particles,
170 mostly electrons, in the orbital environment of a planetary magnetosphere. We suggest that

171 the plume activity at Enceladus could at least partly arise from sporadic interactions of
172 radiolytic oxidants and primordially abundant reductants brought into direct chemical contact
173 within the near-surface (tens of meters to kilometers) environment by internal rheologic
174 processes. Volatile gas products of such reactions, and the primary drivers for cryovolcanic
175 activity, could include CO_2 and CO, commonly found in outgassing from comets, from CH_4
176 oxidation, and N_2 from NH_3 oxidation. Plume neutral gas measurements by the Cassini Ion
177 Neutral Mass Spectrometer (INMS) instrument [*Waite et al.*, 2006] do not distinguish N_2
178 from CO, but if N_2 output is significant as now indicated by recent modelling of data from
179 the Cassini Plasma Spectrometer [*Smith et al.*, 2007], active cryovolcanism and associated
180 outgassing on Enceladus today could be a model for early formation of gravitationally bound
181 N_2 atmospheres on more massive icy bodies such as Titan [*Owen*, 2000; *Niemann et al.*,
182 2005].

183 Laboratory data [*Loeffler et al.*, 2006b] indicate that NH_3 in thin films of water ice reacts
184 strongly with radiolytic products of direct energetic particle irradiation to form N_2 gas, but
185 near-infrared surface measurements [*Brown et al.*, 2006] at Enceladus find no evidence for
186 NH_3 above trace abundances less than one percent relative to H_2O. This low surface
187 abundance is consistent with a similar upper limit 0.5 % reported from neutral plume gas
188 measurements by the Cassini Ion Neutral Mass Spectrometer [*Waite et al.*, 2006]. Any NH_3
189 brought to the surface of Enceladus by rheological transport, or as redeposited to the surface
190 with plume ejecta, is then destroyed rapidly by direct irradiation processes. Absence of NH_3
191 and other reduced compounds above trace levels also means that oxidants can accumulate
192 near the surface without immediate losses to oxidation of these compounds. This
193 circumstance motivates our stratigraphic model (Figure 1) in which oxidant layers are
194 transported downward from the surface to interact with layers of reduced compounds
195 similarly transported upward from deep primordial reservoirs.

196 Chemical energy introduced by radiolytic oxidant production at icy surfaces provides an
197 energy source for cryovolcanic activity and could be particularly effective in warm ice and

198 liquid near-surface environments suggested [*Porco et al.*, 2006; *Spencer et al.*, 2006] for
199 Enceladus. The young geologic age from crater counts in the south polar region [*Porco et al.*,
200 2006], and a current model for polar reorientation by diapirism [Nimmo and Pappalardo,
201 2006], could indicate ongoing material exchange between the irradiated surface, the
202 subsurface source layers for the visible plumes, and the deeper interior. Despite assumptions
203 in other Enceladus plume models to the contrary [*Matson et al.*, 2006], this vertical transport
204 cycle apparently does not extend to the moon's ice mantle boundary with the hot rocky core,
205 since no Europa-like [*McCord et al.*, 1998a, 1998b] mineral salt species from rocky material
206 are detected at the surface. Lack of Europa-like non-ice material extrusion or ejection to the
207 surface, relative to water ice deposition [*Verbiscer et al.*, 2007], is likely why Enceladus
208 maintains its high visual albedo. Similar considerations may apply to internal transport within
209 bright Kuiper Belt Objects, perhaps with darker objects being so due to lesser internal
210 differentiation during primordial formation as compared to the brighter objects.

211 Sublimation of the H_2O ice matrix in the warm [*Spencer et al.*, 2006] (145 K) south polar
212 region could produce high H_2O_2 concentrations [*Loeffler et al.*, 2006a] which could migrate
213 to the subsurface environment in warm ice flows. High solubility of H_2O_2 in liquid H_2O
214 would greatly increase downward and lateral transport rates in near-surface melt water or
215 brine flows and within subsurface water reservoirs. Highly exothermic molecular reactions of
216 the oxidants could occur in liquid phase with a near-surface reservoir of dissolved reductants
217 (e.g., NH_3) in solution with H_2O, or in solid-state phase with hydrate forms of reductants as
218 illustrated in Figure 1. Mixtures of H_2O and H_2O_2 have lower freezing temperatures than
219 pure H_2O and may be energetically favored in early and present cryospheric environments of
220 Earth [*Liang et al., 2006*], Mars [*Schulze-Makuch and Houtkooper*, 2006; *Houtkooper and*
221 *Schulze-Makuch*, 2006], Europa [*Chyba and Hand*, 2001], and elsewhere for biological
222 evolution.

223 The illustration in Figure 1 shows a variety of oxidant and reductant species, but for this
224 report we focus on sequences starting with the catalytic dissociation of H_2O_2 to O_2 in the

presence of a thermal gradient on the ice margin of a subsurface fluid reservoir and of a metal catalyst X. Exothermic reaction sequences can be ignited in H_2O-NH_3 or H_2O-CH_4 mixtures by the hot O_2 from H_2O_2 dissociation. The principal reaction equations and associated exothermic heat outputs are as follows:

$$H_2O_2 + X \rightarrow O_2 \qquad \Delta H_r = 98.2 \text{ kJ/mol } (1.02 \text{ eV/}H_2O_2)$$
$$4NH_3 + 3O_2 \rightarrow 2N_2 + 6H_2O \qquad \Delta H_r = 1359 \text{ kJ/mol } (14.1 \text{ eV/}NH_3)$$
$$CH_4 + 2O_2 \rightarrow CO_2 + 2H_2O \qquad \Delta H_r = 890 \text{ kJ/mol } (9.2 \text{ eV/}CH_4)$$

The activation energy needed to initiate these reactions can be provided in-situ by the initial H_2O_2 dissociation or by catalytic reactions of radicals such as OH or HO_2. The subsequent oxidation of NH_3 and CH_4 respectively forms N_2, CO, or CO_2 gases as drivers for cryovolcanic activity. The H_2O_2 dissociation can be catalysed even in low temperature environments by trace abundances of dissolved transition metal ions (e.g., Ti, V, Fe, Ni, Cu, Zn, Mo). Silver or platinum catalysis of H_2O_2 monopropellent at concentrations of 70 – 98 % in water is used to produce hot (>873 K) steam mixtures of the H_2O and O_2 combustion products in rocket propulsion systems [*Andrews*, 1990]. OH and HO_2 radicals are catalytically produced in the Fenton's Reagent-like transition metal decomposition of H_2O_2. Iron in the form of $FeSO_4$ salt is the typical catalyst for Fenton's Reagent reactions and the metal is universally abundant as a potential catalytic agent for Enceladus. Since we are mainly concerned with visible cryovolvanic activity in the near-surface environments of icy bodies, these low-temperature catalytic reactions may be more directly linked to such activity than high-temperature [*Matson et al.*, 2007] (500 – 800 K) reactions, e.g. for endothermic NH_3 dissociation ($2NH_3 \rightarrow N_2 + 3H_2$), in the deep interior of Enceladus and other icy moons.

Ammonia has not yet been identified at Enceladus from initial Cassini Ion Neutral Mass Spectrometer (INMS) measurements of the neutral plume gas [*Waite et al.*, 2006], but nitrogen as an atomic or molecular ion is certainly present in the magnetospheric plasma of Saturn at the orbit of Enceladus [*Smith et al.*, 2005; *Sittler et al.*, 2005; *Sittler et al.*, 2006]. Cassini Plasma Spectrometer (CAPS) measurements for radial distributions of nitrogen ions are consistent [*Smith et al.*, 2007] with a molecular nitrogen source at Enceladus. Apparent

low abundance <1% of NH_3 in the neutral gas does not rule out presence of ammonia in other forms such as the ammonium ion NH_4^+, highly abundant at neutral pH in H_2O–NH_3 fluid mixtures and indistinguishable from H_2O^+ at the same mass/charge in plasma ion data. Alternatively, H_2O_2 oxidation of NH_3 may be rapid in the fluid state and consistent with absence of these species in the plume gas. As depicted in Figure 1, the primary reaction sites contributing to plume gas production might occur at lower but more sustainable rates in hydrate [*Kieffer et al.*, 2006] phases within warm ice in boundary regions surrounding a central liquid reservoir with the main non-H_2O components being gaseous products of oxidation from these regions.

The advantage of gas-driven fluid flow models for cryovolcanism is that modest molar production rates for gas can lead to much larger mass ejection rates for incompressible fluids. The measured [*Waite et al.*, 2006] volatile gas abundances relative to H_2O at Enceladus correspond to a gas-rich subsurface source environment at a total pressure ~ 10^2 bars. Bubbles of hot, 10^3 K, gas emerging at this pressure into, and rising within, a water reservoir would expand until pressure and temperature equalize with respect to the ambient hydrostatic environment. At the one-bar level, nearly equivalent to one kilometer depth in pure 273 K water at surface gravitational acceleration g ~ 0.1 m s^{-2}, the mass flow ratio of displaced water and N_2 gas is 800:1 as used for the plume flow rates in Table 1. This ratio proportionately increases for declining hydrostatic pressure toward the surface until water depths less than ten meters [*Porco et al.*, 2006] at which sublimation vapour pressure exceeds hydrostatic pressure. Thus a liquid near-surface environment has an advantage in our model of high mass ejection for plume fluid relative to gas production.

Enceladus offers the best available test for cryovolcanic models, since in-situ flyby measurements are available from the ongoing Cassini mission with more planned in the future. At minimum flow speeds of 240 m s^{-1} for gravitational escape, the measured or inferred quantities are H_2O mass loss rates: 3 – 90 kg s^{-1} from direct neutral gas measurements [*Waite et al.*, 2006], 150 – 350 kg s^{-1} from far ultraviolet absorption [*Hansen*

280 *et al.*, 2006], and up to 100 kg s^{-1} from plasma flow deflection by pickup ion mass loading
281 [*Tokar et al.*, 2006]. Averaged over the south polar cap region of area 72,220 km^2 southward
282 of 55°S, these limits respectively correspond to kinetic power, delivered to the subsurface
283 reservoir fluid in our model by oxidation product gases, of 0.001 – 0.04, 0.06 – 0.14, and
284 0.04 mWm^{-2}. Neutral gas data [*Waite et al.*, 2006] also suggest a narrow density spike of
285 mass flow ~0.015 kg s^{-1} near Cassini closest approach. Overall gas data allow a large range
286 of spatial and temporal variability in the flow.

287 As discussed in the next section, the energy fluxes delivered to the south polar region of
288 Enceladus by magnetospheric electron and cosmic ray proton irradiation, and the heat fluxes
289 arising from oxidative reactions, overlap the plume flow power requirements. However, the
290 model gas production rates from radiolytic oxidation are near, or well below, measured lower
291 limits on plume emissions for the product gases and suggest that relatively high abundances
292 of gas have already accumulated in a liquid fluid reservoir after depletion of dissolved NH_3.
293 That is, the current radiolytic oxidant input could maintain the kinetic power of the plume
294 flows but presently be uncorrelated to the cumulative non-H_2O gas composition of the fluid.
295 This suggests a gas-driven cryovolcanic system that is presently in high output phase but that
296 will eventually decline in output as the reservoir gas pressure is released until more gas
297 accumulates as we expect from oxidation of reductant fuels. Since the inflowing chemical
298 energy from radiolysis is continuous, and the potential fuel reservoir from the moon interior
299 is large, there could be many cycles of high and low activity in the familiar pattern of the Old
300 Faithful geyser at Yellowstone National Park on Earth.

301 Another measured quantity from Cassini measurements is the ~80 mWm^{-2} average
302 surface power of the total 5.8 GW thermal emission from the south polar cap [*Spencer et al.*,
303 2006] of Enceladus below 55°S. If this emission level were continuous, our estimates on
304 steady-state radiolytic inputs, as discussed in the next section, would be far too low to
305 account for it. However, even the globally averaged (area = 798,650 km^2) tidal and
306 radiogenic internal heating [*Porco et al.*, 2006], each being about 0.5 GW (0.6 mWm^{-2}) and

307 comparable to the incident energy flux (Table 1) at the global surface from magnetospheric
308 electrons, fall far short as well. The peak temperature of the measured thermal emission at
309 145 K [Spencer *et al.*, 2006] is far too low [e.g., *Matson et al.*, 2007] to ignite the oxidation
310 sequences producing CO_2 and N_2 from hydrocarbons and ammonia, so any direct link
311 between the heat, water plume, and gas emissions remains highly speculative. Since heat may
312 be retained for long intervals within a body of sufficiently low thermal conductivity [*Kargel*,
313 2006], the current thermal emission could be from an earlier transient pulse of high internal
314 heating. Conceivably this heat pulse might have created or expanded the putative liquid
315 reservoir. The enhanced thermal environment would not directly create cryovolcanic gases
316 but would do so indirectly through acceleration of catalytic reactions such as we discuss for
317 the radiolytic model.

318 Radiolytic oxidant accumulation in the ice crust over tens of thousands of years or longer
319 could account for transient heat emission and plume activity even at current levels, e.g. if
320 large clumps of peroxide-saturated ice had recently come into contact with concentrations of
321 ammonia or other fuels as illustrated in Figure 1. The relatively distinct layers of oxidants and
322 frost depicted in this figure would break up into clumpier concentrations during downward
323 rheological transport and could aggregate into distributions of many smaller clumps and some
324 large clumps over time. Lower freezing temperature of H_2O_2-enriched ice could produce
325 more concentrated pockets of H_2O_2 over successive local melting and freezing cycles in the
326 vicinity of the liquid reservoir. Relatively explosive activity may explain the large increase of
327 February 2004 in neutral oxygen density observed via ultraviolet emissions [*Esposito et al.*,
328 2005] as Cassini approached the Saturn system. The inferred doubling of E-ring mass by
329 5×10^8 kg and subsequent dissipation to previous mass level over a two-month period is
330 equivalent to Enceladus outgassing at 100 kg/s over this same period.

331 **Energy Input and Gas Production**

332 The Cassini Orbiter has now flown several times across the jovicentric orbit of Enceladus,
333 but measurements of the energetic particle flux environment at the orbit of this moon are also
334 available from the past Pioneer 11 and Voyager 2 Saturn flybys. Representative flux spectra
335 for the magnetospheric radiation environment of Enceladus and other icy moons of Saturn
336 have been incorporated from the Pioneer and Voyager data into the SATRAD model [*Garrett*
337 *et al.*, 2005] developed by NASA's Jet Propulsion Laboratory. The electron flux spectra from
338 SATRAD are plotted in Figure 2 for the local magnetospheric environments of Mimas,
339 Enceladus, Tethys, Dione, and Rhea. The respective integrated energy fluxes above 10 keV
340 for these moons are 2.5, 0.7, 0.5, 0.4, and 0.3 mW/m^2, so Enceladus's radiation environment
341 is of intermediate intensity in the Saturn magnetosphere.

342 In comparison, the energy flux at Europa in the Jupiter magnetosphere is forty times
343 higher [*Cooper et al.*, 2001] even than at Mimas, and yet there is no evidence thus far for
344 ongoing cryovolcanism or any other surface activity there [*Phillips et al.*, 2000]. High
345 radiation energy flux at icy moon surfaces is evidently not sufficient to produce visible plume
346 activity. The present cryovolcanic model further requires radiolytic product access from the
347 irradiated surface to subsurface deposits of reductant fuels such as ammonia and methane.
348 Cassini magnetometer data on ion cyclotron waves suggest a weaker ion source at Dione by a
349 factor of 300 as compared to Enceladus [*Leisner et al.*, 2007]. In the context of the radiolytic
350 model this difference is either due to correspondingly lower abundance of reductants in the
351 upper ice crust of Dione, or to absence of a liquid subsurface reservoir in the event that
352 reductant abundances are similar to those of Enceladus.

353 For Enceladus the SATRAD spectrum, shown again in Figure 3, provides a useful median
354 sample of the moon's radiation environment even over the twenty-eight years since the
355 Pioneer 11 flyby in 1979. Figure 3 additionally shows current low and high limits for flux
356 distributions of electrons at Enceladus. A collection of other measured MIMI spectra is also
357 included from several other traversals of the moon's orbit around Jupiter. These assorted
358 measurements are mostly well bounded by the upper and lower limit spectra.

359 Integrated input energy, H_2O_2 production, oxidative heat, and N_2 gas fluxes from these
360 distributions are listed in Table 1 for catalyzed exothermic dissociation of H_2O_2 to O_2 and
361 subsequent exothermic oxidation of NH_3 to H_2O and N_2 gas. For these estimates we use the
362 maximum measured radiolytic yield, G = 0.4, a reasonable upper limit from laboratory data
363 [*Moore and Hudson*, 2000] for an ice crust potentially saturated with CO_2 and O_2 products of
364 radiolytic chemistry. The plume flow rates in Table 1 are computed for N_2 gas displacement
365 of H_2O fluid at the 1-bar pressure (1-km fluid depth) level.

366 The lower limits on incident energy flux come from the Cassini's Enceladus I flyby, and
367 fluxes were substantially higher a quarter century ago during the Pioneer and Voyager flybys.
368 Subsequent Cassini data show variable fluxes up to the SATRAD level. As a primary source
369 of neutral gas for the Saturn magnetosphere, high plume output may suppress, via energy loss
370 through atomic ionisation, the low-energy seed population of energetic electrons in the
371 magnetosphere. Depletion of low energy plasma electrons in the inner magnetosphere was
372 earlier found by Voyager as a direct indicator of electron energy loss in the E-ring and
373 associated neutral gas environment [*Sittler et al.*, 1981]. The electron fluxes in Figure 3 are
374 measured away from the moon and are representative of globally averaged irradiation at the
375 surface but would vary there with longitude and latitude location. Magnetospheric magnetic
376 fields [*Dougherty et al.*, 2006] and plasma flow [*Tokar et al.*, 2006] appear significantly
377 perturbed around Enceladus, so energy flux at the surface may concentrate at higher values,
378 e.g. by a factor of two, in the polar regions with reduced values at the equator. Enhancement
379 of more dense or amorphous H_2O_2 ice in the tiger stripes region [*Newman et al.*, 2006] is
380 consistent with polar focusing of the magnetospheric particle fluxes.

381 Comparative incident flux distributions are also shown in Figure 3, along with
382 corresponding energy flux values in Table 1, for electrons at Europa [*Cooper et al.*, 2001]
383 and for cosmic ray proton irradiation of Saturn's main rings [*Johnson et al.*, 2006] and of
384 other icy objects [*Cooper et al.*, 2003; *Cooper et al.*, 2006] in the outer heliosphere (40 AU,
385 heliosheath) and local interstellar medium. Cosmic ray interactions with Saturn's ring

386 material partly accounts for the observed oxygen atmosphere of these rings through total
387 oxidant production. The dominant oxidant energy source in the rings is presently thought to
388 be solar ultraviolet irradiation [*Johnson et al.*, 2006], and, based on earlier work for Europa
389 [*Cooper et al.*, 2001], we estimate ~ 0.014 mWm^{-2} as the contribution of this radiation
390 component at the south polar cap (south of 55°S) of Enceladus. Extrapolation of the cosmic
391 ray energy flux through Saturn's planetary magnetic field to Enceladus gives an approximate
392 surface contribution there well below the contribution limits from magnetospheric electrons
393 but extending more deeply into the surface. Total UV and cosmic ray energy flux
394 contributions at the Enceladus polar cap are then of order 0.02 – 0.03 mWm^{-2}, one to two
395 orders of magnitude below the magnetospheric electron input.

396 The depth profiles of time scales for accumulation of radiolytic dosages computationally
397 sufficient to convert 90% of all irradiated H_2O ice molecules to H_2O_2 at G = 0.4 are shown in
398 Figure 4 for the electron and proton flux spectra in Figure 3. Within the visibly sensible layer,
399 less than 1 mm in depth for inferred ice grain sizes of order 10^2 μm [*Brown et al.*, 2006], the
400 time scales are 10^5 years for Enceladus, 10^3 years for Europa, and $10^8 - 4x10^9$ years for the
401 outer heliosphere and beyond. Complete conversion to H_2O_2 in the visible layer can therefore
402 occur on moon and minor planet icy bodies, photolytic destruction and other losses being
403 ignored, over time scales from those of terrestrial ice ages and glacial flow times to the solar
404 system age.

405 On Enceladus the 10^7-year turnover of the meter-thick icy regolith layer, as approximated
406 from a Europa model [*Cooper et al.*, 2001] of impact gardening, produces a peroxide fraction
407 to water ice of nearly 10% in this layer. Paucity of large impact craters in the south polar
408 region [*Porco et al.*, 2006] indicates continual resurfacing to kilometers in depth. Over the
409 solar system age, up to ~50 m of water ice at G = 0.4 is then converted to H_2O_2 on Enceladus
410 as compared to ~5 km within Europa's surface and to 20 cm for Kuiper Belt Objects and
411 Saturn's rings. These values suggest that the upper ice crusts of both Enceladus and Europa,
412 and much of the sensible and deeper impact regolith layers on KBOs, could be saturated with

413 H_2O_2 and other oxidants. Since the condensed thickness of Pluto's ~10-microbar N_2
414 atmosphere [*Elliot et al.*, 2003] is equivalent in mass to ~0.1 cm of H_2O_2, the much thicker
415 radiolytic accumulation of H_2O_2 there may have a significant chemical impact on the
416 atmospheric evolution of Pluto. Higher surface thicknesses ~ 10 cm to 100 m for N_2 ice on
417 Triton [*Cruikshank et al.*, 1984], the other site of directly observed cryovolcanic activity,
418 could easily arise from radiolytic chemistry, since that moon orbits Neptune within a hot
419 plasma magnetospheric environment. Neptunian energetic electrons and protons provide 10^9
420 W energy input to Triton auroral excitation [*Krimigis et al.*, 1990] as compared to our upper
421 limit of 1.5×10^8 W from Saturnian electrons at the south polar cap of Enceladus. Greater
422 distance from the Sun at Triton would further increase relative importance of the local
423 radiolytic energy source as compared to previously discussed solar energy sources for the
424 Triton N_2 geysers.

425 Finally, limits on N_2 gas mass flux up to 0.08 kg s^{-1} from H_2O_2 dissociation to O_2 and
426 NH_3 oxidation are given in Table 1 for all cases. Incompressible fluid displacement factors
427 10^3 or greater from the N_2 mass flux at fluid depths less than 1 km, the one-bar pressure
428 level, are then sufficient to produce observed total plume mass flows $10^1 - 10^2$ kg s^{-1}.
429 However, the Cassini INMS [*Waite et al.*, 2006] measured upper limits ~0.2 – 6 kg s^{-1} for the
430 measured number ratio N_2:H_2O of 0.04:1.0 of Enceladus plume gas are well above even the
431 upper limit of steady-state production from the radiolytic model.

432 Since the energy and heat fluxes in Table 1 are comparable to limits on the plume kinetic
433 power, the disparity in gas fluxes suggests a lack of direct coupling between radiolytic gas
434 injection and plume gas ejection. Together with low measured limits from INMS on
435 abundance of NH_3 in the plume gas, this disparity may indicate that the plume gas is
436 originating from a gas-saturated subsurface environment in which local abundances of NH_3
437 near the liquid reservoir have recently been depleted by cumulative oxidation. Apparent lack
438 of H_2O_2 in the plume gas, if we assume for the moment that INMS has any significant
439 sensitivity to such reactive species, similarly argues that H_2O_2 and NH_3 react mainly in the

440 boundary regions surrounding the putative liquid reservoir and that only the gaseous
441 oxidation products persist in that reservoir. Future improvements in laboratory calibration of
442 INMS with respect to reactive oxidants may change this assessment. Unless the plumes are
443 unique to the present epoch, the depleted NH_3, also including that part lost at the surface by
444 direct irradiation [*Loeffler et al.*, 2006b], must eventually be resupplied by upward transport
445 of NH_3 - rich ice from the deep interior.

446 **Discussion**

447 The radiolytic model depends on the near-surface production of oxidants that should be
448 present near the surface of icy bodies of the outer solar system, wherever water ice is
449 irradiated by energetic particles and ultraviolet photons from the magnetospheric,
450 heliospheric, or interstellar space environments of these bodies. Chemical energy
451 accumulates in these oxidants over a vast range of time scales in different magnetospheric,
452 and heliospheric, locations. This energy can be released when the oxidants come into contact
453 with reductant fuels such as NH_3 and CH_4 in the presence either of high temperatures or
454 catalytic materials Hydrogen peroxide is produced by ice radiolysis and photolysis in low-
455 temperature environments and has the advantage of exothermic, potentially explosive,
456 dissociation to O_2 in the presence of iron and other commonly abundant metal catalysts. No
457 laboratory measurements are yet available on metal-catalyzed dissociation rates at the
458 observed temperatures of 80 – 145 K on Enceladus but these rates would rapidly increase in
459 the warmer ice surrounding a liquid water reservoir. This initial exothermic reaction could
460 then initiate oxidation of reductants to produce volatile gases driving cryovolcanic activity.
461 Trace hydrocarbon species, such as the INMS-detected [*Waite et al.*, 2006] acetylene and
462 propane at Enceladus, could be produced in the high temperature sequences initiated by H_2O_2
463 dissociation. These species may take part in further reactions, potentially with explosive
464 results, as found by Benit and Roessler [1993] for proton-irradiated acetylene frost at 77 K,
465 even at the low end of the Enceladus temperature range.

466 Visible manifestations of cryovolcanism include emissions of ice grains, neutral gas,
467 pickup ions, and dust, but the generally bright reflective surfaces of other icy bodies, as in the
468 Kuiper Belt, are also highly suggestive of sustained cryovolcanism. New observations of
469 ammonia hydrate on the surface of Charon in the Pluto system [*Cook et al.*, 2007] suggest
470 that cryovolcanism is active there. In the Saturn magnetospheric environment the Enceladus
471 ice grain output sustains the E-ring population which then globally bombards and brightens
472 [*Verbiscer et al.*, 2007] the surfaces of Enceladus and other moons. Cyclic activity at
473 Enceladus could produce stratigraphic layers (Figure 1) of high oxidant accumulation during
474 low activity intervals and of high albedo water frost from direct plume output and surface
475 bombardment by E-ring grains during high activity phases. Currently high plume and thermal
476 emission suggests that Enceladus is now in its most active phase, and that any non-ice
477 materials, including abundant oxidants expected from continuous magnetospheric irradiation,
478 are now mostly buried from view by water ice frost from plume ejecta.

479 Enceladus outgassing into Saturn's magnetosphere, and resultant electron energy loss in E-
480 ring dust and neutral gas, should lead to anti-correlation of plume output with the fluxes of
481 energetic and lower-energy suprathermal electrons near and beyond the orbit of Enceladus.
482 The large decrease in low energy (< 0.5 MeV) electron and energetic (> 0.5 MeV) ion fluxes
483 inward from the orbit of Rhea (8.75 R_S) to that of Enceladus (3.75 R_S) was first discovered
484 by Pioneer 11 measurements [*McDonald et al.*, 1980; *Simpson et al.*, 1980; *Trainer et al.*,
485 1980; *Van Allen et al.*, 1980]. The subsequent Voyager measurements found dropouts in
486 suprathermal (0.03 – 6 keV) electron [*Sittler et al.*, 1981], ring current ion [*Connerney et al.*,
487 1981; *Acuña et al.*, 1981], and energetic (> 500 keV) ion [*Krimigis et al.*, 1981, 1983; and as
488 reinterpreted by *Paranicas et al.*, 2004] fluxes.

489 These inward flux decreases are now clearly attributable to Enceladus neutral gas and E-
490 ring ice grain interactions a quarter century after the first suggestion of a potential E-ring
491 interaction by Thomsen and Van Allen [1979] in a report published just after the Pioneer 11
492 flyby. In comparison, the Pioneer and Voyager energetic electron fluxes increased with no

493 evident E-ring interaction toward Saturn, until cutoff by the main rings, from source regions
494 in the Enceladus – Rhea region and beyond. Generally reduced fluxes of energetic electrons
495 near the orbit of Enceladus, as recently measured by the Cassini MIMI instrument (Figure 3),
496 suggest that the currently high plume output may be attenuating the supply of low-energy
497 electrons feeding via magnetospheric acceleration processes into the energetic electron
498 population. If so, the current rate of surface oxidant production is now low but will again
499 increase if plume output subsides and the low-energy electron source of the energetic
500 electrons at Enceladus is no longer attenuated in diffusing inward through the E-ring region.

501 Negative feedback of Enceladus plume activity to the electron source could produce cyclic
502 high phases of "Old Faithful" activity initiated after long periods of high oxidant
503 accumulation rates during low activity phases. Cyclic plume activity elsewhere may be
504 confined to planetary magnetospheric environments in which the cryovolcanic emissions are
505 large enough to attenuate source fluxes of energetic particles producing the surface oxidants.
506 In heliospheric environments the activity may be more episodic and driven by subsurface
507 circulation of reductant fuels to the oxidant-saturated near-surface water ice environment. In
508 all cases, interactions of clumps of highly concentrated oxidants and reductants, as in Figure
509 1 for Enceladus, could produce transiently high plume activity and heat output after slow
510 accumulations over much longer time intervals, e.g. thousands of years for Enceladus as
511 compared to the quarter-century of our present Voyager-Cassini measurements for the E-ring
512 and now for Enceladus. In comparison, long term storage of heat, e.g. due to low thermal
513 conductivity in the ice mantle [*Kargel*, 2006], can be theorized for alternative theories
514 invoking episodic tidal heating, but we have yet no independent evidence for such episodes in
515 the surface features and chemical composition of Enceladus.

516 Enceladus has the highest density, 1.6 g/cc, of all major Saturn satellites excluding Titan,
517 but the sensible surface does not show composition consistent with continuing chemical
518 contact to the requisite rocky core [*Porco et al.*, 2006] underlying the outer ice mantle at this
519 density. There is no evidence from near-infrared imaging spectroscopy [*Brown et al.*, 2006]

520 for surface presence of Europa-like [*McCord et al.*, 1998a, 1998b] sulfate hydrates or other
521 non-ice species that might directly convect through warm ice crust layers to the surface or
522 become manifested through the plume outflow. We suggest that this poses a significant
523 problem for the widely publicized theory of *Matson et al.* [2007] that the plumes are a
524 manifestation of high temperature (> 500 K) ammonia chemistry and resultant gas production
525 deep in the moon interior at the core-mantle boundary. A deep source is also difficult to
526 connect to plume variability strongly suggested by the large transient increase [*Esposito et*
527 *al.*, 2005] in magnetospheric neutral gas during Feb. 2004. Such transients are more likely to
528 arise from plume source dynamics closer to the surface.

529 We acknowledge the suggestions of *Kargel* [2006] and *Kieffer et al.* [2006] that gas
530 clathrate decomposition in the presence of thermal gradients could contribute to Enceladus
531 cryovolcanism, but production of the enclathrated gases then remains to be explained. If
532 formed during original accretion and differentiation of Enceladus, these gases would have
533 long since escaped, since this moon is too small to retain an atmosphere like that of Titan
534 [*Owen*, 2000]. Sequestration of the ammonia in rocky ammonium minerals was suggested as
535 one alternative [*Kargel*, 2006], but lack of surface compositional expression for continuous
536 ice mantle circulation from the rock core boundary provides no current support for this
537 alternative. The radiolytic model instead postulates that primordial ammonia, methane, and
538 other hydrocarbon sources of cryovolcanic gases are abundant within the ice mantle, e.g. in
539 the form of hydrates, and that gas production occurs in the warm ice basal margins of a near-
540 surface liquid reservoir on contact with oxidants from the irradiated surface.

541 Even at the relatively high temperature of pure liquid water, the spontaneous dissociation
542 of H_2O_2 to O_2 must be catalysed in the radiolytic model by non-ice contaminants, e.g.
543 universally abundant Fe, originating either from the rocky mineral composition of the deep
544 interior or from meteoritic bombardment. The absences of detectable minerals on the surface
545 and of O_2 in the atmospheric environment argue that this dissociation cannot occur very near
546 the surface, and that radiolytic H_2O_2 can continuously accumulate and concentrate in the

547 near-surface ice environment. If the near-surface environment undergoes cyclic melting and
548 freezing phases, the non-ice materials will accumulate as brines at lower depths below the
549 melt layers. These contaminants will similarly have low abundances within a liquid
550 subsurface reservoir and likely contribute only at trace levels to composition of cryovolcanic
551 plumes. For the present model we assume that sufficient trace abundances of Fe and other
552 metals are mixed with continuously upwelling fuels, e.g. hydrates of NH_3 and CH_4, to trigger
553 H_2O_2 dissociation at the basal thermal margins of the fluid reservoir as depicted in Figure 1,
554 and that these metals do not limit the accumulation of H_2O_2 above the reservoir. This vertical
555 gradient in catalyst density allows the requisite inverse gradient in oxidant accumulation to
556 occur and sets the stage for the exothermic reactions leading to gas production and fluid
557 ejection to form cryovolcanic plumes. Initial vertical segregation of oxidants and fuels may
558 be essential to the explosive form of cryvolcanism potentially accounting for the spectacular
559 plumes of Enceladus.

560 Saturn kilometric radiation (SKR) provides a new diagnostic for limits on magnetospheric
561 mass loading by ions originating from Enceladus plume gas and ice grains. During the 1980 –
562 1981 flybys the two Voyager spacecraft discovered these radio emissions with a periodicity
563 of 10 hours 39 min 24 ± 7 s, then thought to arise from intrinsic rotation of Saturn [*Desch*
564 *and Kaiser*, 1981]. Later Ulysses radio observations from 1994 to 1997 showed changes in
565 SKR periodicity up to 1% relative to the Voyager observations. Initial Cassini measurements
566 determined a more precise value of 10 hours 45 min 45±36 s [*Gurnett et al.*, 2005] for an
567 increase of 6.35 minutes (1%) since 1980 - 1981. Slippage of the coupled magnetosphere-
568 ionosphere system with respect to planetary rotation, due to magnetospheric plasma loading
569 by Enceladus outgassing and subsequent ionisation of plume neutrals, is proposed [*Gurnett et*
570 *al.*, 2007] to account for the radio SKR period. A theory of rotationally-driven plasma
571 convection [*Goldreich and Farmer*, 2006] estimates the mass loading for the 1% SKR period
572 variation at 10 kg/s radial mass outflow from Enceladus and the E-ring. Although zonal

573 variations of Saturn's atmospheric rotation speeds presently preclude independent
574 measurement of intrinsic planetary rotation, differential changes in SKR period could be
575 monitored as a linear measure of Enceladus plume output. Stability of this period within 1%
576 does imply relative stability over the last quarter century but does not limit longer term
577 stability. Continued monitoring of SKR periodicity, as compared to Enceladus plume activity
578 and magnetospheric particle fluxes, is needed to further quantify Enceladus two-way
579 coupling to the magnetosphere.

580 The current plume flow limits of 3 - 350 kg/s for Enceladus project over the solar system
581 age to the cumulative loss of 0.4 – 46 % from the moon's total mass. For spherical symmetry
582 a flow rate of 70 kg/s extrapolates to complete loss of the nine percent of total moon mass
583 southward of 55°S. Enormous redistribution of mass would have globally occurred within the
584 deep interior if the plumes had been continuously active at such rates. A far lower limit on
585 cumulative mass loss of 0.03%, corresponding to 0.2 kg/s in flow rate, comes from the
586 observed ~ 0.5-km depression of the south polar cap region [*Porco et al.*, 2006], although
587 much of the plume mass has likely returned to the surface. Thus the average flow rate may
588 have been even much lower even than 3 kg/s, and there could have been long intervals for
589 accumulation of stored radiolytic energy to fully account for all aspects of current plume flow
590 and polar cap heat emission. The present epoch of high activity, manifested in the E-ring
591 during the Voyager era of 1980 – 1981, and now seen directly by Cassini, may be a short-
592 lived and periodic event over the history of Enceladus. An apt analogy may be Old Faithful
593 with variable output eruptions over a few minutes at intervals of about ninety minutes. It is
594 therefore now advisable to calibrate remote long-term indicators of plume activity, potentially
595 including SKR emission that be monitored from Earth, to the ongoing Cassini measurements
596 within the Saturn system.

597 Oxidant chemistry induced by cosmic ray irradiation could drive resurfacing on the large
598 bright Kuiper Belt Objects such as Eris and more generally account for the diversity of
599 surface brightness and color [*Jewitt and Luu*, 2001; *Doressoundiram et al.*, 2002] among the

600 icy dwarf planets of the outer solar system. Water ice mantles should be common on KBOs
601 and deep water-ice absorptions are directly seen on some objects such as the 2003 EL_{61}
602 collisional family [*Brown et al.*, 2007; *Barkume et al.*, 2006] and Charon [*Brown and Calvin*,
603 2000]. Although N_2 and CH_4 ices are dominant on larger bodies such as Pluto [*Brown and*
604 *Calvin*, 2000] and Eris [*Brown et al.*, 2005], surface layers of these volatile molecules would
605 not be retained on smaller objects [*Brown and Calvin*, 2000] and, if present, would have to be
606 renewed by outgassing from the subsurface, e.g. by cryovolvanism. Oxidant production from
607 cosmic ray irradiation of visible surface or near-surface water ice must therefore be
608 accounted for as one chemical energy source for potential cryovolcanic activity of these
609 objects. The respective Voyager 2 and Cassini flyby observations have given the first close
610 looks at active cryovolcanism on Triton and Enceladus. New Horizons is our next
611 opportunity to search for such activity at Pluto and Charon during the April 12, 2015 flyby of
612 this icy dwarf planet system.

613 Finally, the suggested vertical segregation of near-surface radiolytic oxidants and deeper-
614 lying reductant fuels on irradiated icy bodies potentially provides chemical energy resources
615 for future exploration and habitation of the outer solar system and beyond. Since heliocentric
616 orbits of many of these bodies, such as Centaurs, are dynamically unstable, oxidant and fuel
617 mining can be envisaged on icy objects having more recently entered the inner solar system
618 after billions of years of radiolytic processing in the Kuiper Belt or Oort Cloud regions. If
619 there is ever the need to divert such an object from impact with the Earth, this potentially
620 accessible chemical redox energy accumulated within the body could become a critical
621 resource. In these respects, if the radiolytic model proves to be correct, Enceladus may be
622 viewed not only as an object of intense scientific interest but also as a natural model for
623 astroengineering. Sagan [1994] suggested utilization of icy bodies as spaceships to other
624 stars, and Enceladus may be a spectacularly visible model for fulfilment of this vision.

625

625 **References**

626 Acuña, M. H., J. E. P. Connerney, and N. F. Ness (1981), Topology of Saturn's main
627 magnetic field, *Nature*, *292*, 721-724.

628 Andrews, D. (1990), Advantages of hydrogen peroxide as a rocket oxidant, *J. Brit. Interplan.*
629 *Soc.*, *43*, 319-328.

630 Barkume, K. M., M. E. Brown, and E. L. Schaller (2006), Water ice on the satellite of Kuiper
631 belt object 2003 EL_{61}, *Astrophys. J.*, *640*, L87-L89.

632 Benit, J., and K. Roessler (1993), Explosive processes in frozen acetylene irradiated by MeV
633 protons (cosmic ray simulation), in *Astronomical Infrared Spectroscopy: Future*
634 *observational directions*, edited by S. Kwok, *ASP Conf. Ser. 41*, pp. 277-278, Astron. Soc.
635 Pacific.

636 Brown, M. E, and W. M. Calvin (2000), Evidence for crystalline water and ammonia ices on
637 Pluto's satellite Charon, *Science*, *287*, 107-109.

638 Brown, M. E., C. A. Trujillo, and D. L. Rabinowitz (2005), Discovery of a planetary-sized
639 object in the Scattered Kuiper Belt, *Astrophys. J. Lett.*, *635*, L97-L100.

640 Brown, R. H., R. L. Kirk, T. V. Johnson, and L. A. Soderblom (1990), Energy sources for
641 Triton's geyser-like plumes, *Science*, *250*, 431-435.

642 Brown, R. H., et al. (2006), Composition and physical properties of Enceladus' surface,
643 *Science*, *311*, 1425-1428.

644 Brown, M. E., K. M. Barkume, D. Ragozzine, and E. L. Schaller (2007), A collisional family
645 of icy objects in the Kuiper Belt, *Nature*, *446*, 294-296.

646 Buratti, B. J., et al. (2005), Cassini Visual and Infrared Mapping Spectrometer observations
647 of Iapetus: Detection of CO_2, *Astrophys. J.*, *622*, L149-L152.

648 Carlson, R. W. (1999), A tenuous carbon dioxide atmosphere on Jupiter's moon Callisto,
649 *Science*, *283*, 820-821.

650 Carlson, R., et al. (1999), Hydrogen peroxide on the surface of Europa, *Science*, *283*, 2062-
651 2064.
652 Chyba, C. F., and K. P. Hand (2001), Life without photosynthesis, *Science*, *292*, 2026-2027.
653 Connerney, J. E. P., M. H. Acuña, and N. F. Ness (1981), Saturn's ring current and inner
654 magnetosphere, *Nature*, *292*, 724-726.
655 Cook, J. C., S. J. Desch, T. L. Roush, C. A. Trujillo, and T. R. Geballe (2007), Near-infrared
656 spectroscopy of Charon: Possible evidence for cryovolcanism on Kuiper Belt Objects,
657 *Astrophys. J.*, *663*, 1406–1419.
658 Cooper, J. F., R. E. Johnson, B. H. Mauk, H. B. Garrett, and N. Gehrels (2001), Energetic ion
659 and electron irradiation of the icy Galilean satellites, *Icarus*, *149*, 133-159.
660 Cooper, J. F., E. R. Christian, J. D. Richardson, and C. Wang (2003), Proton irradiation of
661 Centaur, Kuiper Belt, and Oort Cloud objects at plasma to cosmic ray energy, *Earth Moon*
662 *Plan.*, *92*, 261-277.
663 Cooper, J. F., M. E. Hill, J. D. Richardson, and S. J. Sturner (2006), Proton irradiation
664 environment of solar system objects in the heliospheric boundary regions, in *Physics of the*
665 *Inner Heliosheath, Voyager Observations, Theory, and Future Prospects; 5th Annual*
666 *IGPP International Astrophysics Conference*, edited by J. Heerikhuisen, V. Florinski, G.P.
667 Zank and N.V. Pogorelov, *AIP Conf. Proc. 858*, pp. 372-379.
668 Cruikshank, D. P., R. H. Brown, and R. G. Clark (1984), Nitrogen on Triton, *Icarus*, *58*, 293-
669 305.
670 Cruikshank, D. P., T. L. Roush, J. M. Moore, M. Sykes, T. C. Owen, M. J. Bartholomew,
671 R. H. Brown, and K. A. Tryka (1997), The surfaces of Pluto and Charon, in *Pluto and*
672 *Charon*, edited by S. A. Stern, and D. J. Tholen, p. 211, University of Arizona Press,
673 Tucson.

674 Divine, N., and H. B. Garrett (1983), Charged particle distributions in Jupiter's
675 magnetosphere, *J. Geophys. Res.*, *88*, 6889–6903.
676 Doressoundiram, A., N. Peixinho, C. de Bergh, S. Fornasier, Ph. Thébault, M. A. Barucci,
677 and C. Veillet (2002), The color distribution in the Edgeworth-Kuiper Belt, *Astron. J.*,
678 *124*, 2279-2296.
679 Dougherty, M. K., K. K. Khurana, F. M. Neubauer, C. T. Russell, J. Saur, J. S. Leisner, and
680 M. E. Burton (2006), Identification of a dynamic atmosphere at Enceladus with the Cassini
681 Magnetometer, *Science*, *311*, 1406-1409.
682 Esposito, L., et al. (2005), Ultraviolet imaging spectroscopy shows an active Saturnian
683 system, *Science*, *307*, 1251-1255.
684 Formisano, V., S. Atreya, T. Encrenaz, N. Ignatiev, and M. Giuranna (2004), Detection of
685 methane in the atmosphere of Mars, *Science*, 306, 1758-1761.
686 Garrett, H. B., J. M. Ratliff, and R. W. Evans (2005), Saturn Radiation (SATRAD) Model,
687 JPL Pub. 05-09, NASA Jet Propulsion Lab.
688 Goldreich, P., and A. J. Farmer (2006), Spontaneous axisymmetry breaking of Saturn's
689 external magnetic field, *J. Geophys. Res.*, *112*, A05225, doi:10.1029/2006JA012163.
690 Gomis, O., G. Leto, and G. Strazzulla (2004a), Hydrogen peroxide production by ion
691 irradiation of thin water ice films, *Astron. Astrophys.*, *420*, 405-410.
692 Gomis, O., M. A. Satorre, G. Strazzulla, and G. Leto (2004b), Hydrogen peroxide formation
693 by ion implantation in water ice and its relevance to the Galilean satellites, *Plan. Sp. Sci.*,
694 *52*, 371-378.
695 Gurnett, D. A., A. M. Persoon, W. S. Kurth, J. B. Groene, T. F. Averkamp, M. K. Dougherty,
696 and D. J. Southwood (2007), The variable rotation period of the inner region of Saturn's
697 plasma disk, *Science*, *316*, 442-445.

698 Hall, D. T., D. F. Strobel, P. D. Feldman, M. A. McGrath, and H. A. Weaver (1995),
699 Detection of an oxygen atmosphere on Jupiter's moon Europa, *Nature*, *373*, 677-679.
700 Hall, D. T., P. D. Feldman, M. A. McGrath, and D. F. Strobel (1998), The far-ultraviolet
701 oxygen airglow of Europa and Ganymede, *Astrophys. J.*, *499*, 475-481.
702 Hansen, C. J., L. Esposito, A. I. F. Stewart, J. Colwell, A. Hendrix, W. Pryor, D.
703 Shemansky, and R. West (2006), Enceladus' water vapor plume, *Science*, *311*, 1422-1425.
704 Hendrix, A. R., C. A. Barth, and C. W. Hord (1999a), Ganymede's ozone-like absorber:
705 Observations by the Galileo ultraviolet spectrometer, *J. Geophys. Res.*, *104*, 14169-14178.
706 Hendrix, A. R., C. A. Barth, A. I. F. Stewart, C. W. Hord, and A. L. Lane (1999b), Hydrogen
707 peroxide on the icy Galilean satellites, paper presented at 30th Annual Lunar and Planetary
708 Science Conference, March 15-29, 1999, Houston, TX, Abstract No. 2043.
709 Hibbitts, C. A., T. B. McCord, and G. B. Hansen (2000), Distributions of CO_2 and SO_2 on the
710 surface of Callisto, *J. Geophys. Res.*, *105*, 22541-22557.
711 Hibbitts, C. A., J. E. Klemaszewski, T. B. McCord, G. B. Hansen, and R. Greeley (2002),
712 CO_2-rich impact craters on Callisto, *J. Geophys. Res.*, *107*, 5084,
713 doi:10.1029/2000JE001412.
714 Hibbitts, C. A., R. T. Pappalardo, G. B. Hansen, and T. B. McCord (2003), Carbon dioxide
715 on Ganymede, *J. Geophys. Res.*, *108*, 5036, doi:10.1029/2002JE001956.
716 Houtkooper, J. M., and D. Schulze-Makuch (2007), A possible biogenic origin for hydrogen
717 peroxide on Mars: the Viking results reinterpreted, *Int. J. Astrob.*, *6*, 147-152.
718 Jewitt, D. C., and J. X. Luu (2001), Colors and spectra of Kuiper Belt objects, *Astron. J.*, *122*,
719 2099-2114.
720 Johnson, R. E., R. W. Carlson, J. F. Cooper, C. Paranicas, M. H. Moore, and M. C. Wong
721 (2004), Radiation effects on the surfaces of the Galilean satellites, In *Jupiter - The Planet,*

722 *Satellites and Magnetosphere*, edited by F. Bagenal, W. B. McKinnon, and T. E. Dowling,
723 pp. 485-512, Cambridge Univ. Press, New York.
724 Johnson, R. E., J. G. Luhmann, R. L. Tokar, M. Bouhram, J. J. Berthelier, E. C. Sittler, J. F.
725 Cooper, T. W. Hill, H. T. Smith, M. Michael, M. Liu, F. J. Crary, and D. T. Young
726 (2006), Production, ionization and redistribution of O_2 in Saturn's ring atmosphere, *Icarus*,
727 *180*, 393-402.
728 Kargel, J. S. (2006), Enceladus: Cosmic gymnast, volatile miniworld, *Science*, *311*, 1389-
729 1391.
730 Kieffer, S. W., X. Lu, C. M. Bethke, J. M. Spencer, S. Marshak, and A. A. Navrotsky (2006),
731 Clathrate reservoir hypothesis for Enceladus' south polar plume, *Science*, *314*, 1764-1766.
732 Kirk, R. L., R. H. Brown, and L. A. Soderblom (1990), Subsurface energy storage and
733 transport for solar-powered geysers on Triton, *Science*, *250*, 424-429.
734 Kivelson, M. G., F. Bagenal, W. S. Kurth, F. M. Neubauer, C. Paranicas, and J. Saur (2004),
735 Magnetospheric interactions with satellites, In *Jupiter - The Planet, Satellites and*
736 *Magnetosphere*, edited by F. Bagenal, W. B. McKinnon, and T. E. Dowling, pp. 513-536,
737 Cambridge Univ. Press, New York.
738 Krimigis, S. M., et al. (1989), Hot plasma and energetic particles in Neptune's
739 magnetosphere, *Science*, *246*, 1483-1489.
740 Krimigis, S. M., et al. (2004), Magnetosphere Imaging Instrument (MIMI) on the Cassini
741 Mission to Saturn/Titan, *Sp. Sci. Rev.*, *114*, 233-329.
742 Leisner, J. S., K. K. Khurana, C. T. Russell, M. K. Dougherty, A. M. Persoon, X. Blanco-
743 Cano, and R. J. Strangeway (2007), Observations of Enceladus and Dione as sources for
744 Saturn's neutral cloud, paper presented at 38th Annual Lunar and Planetary Science
745 Conference, Houston, TX, Abstract No. 1425.

746 Liang, M.C., B. F. Lane, R. T. Pappalardo, M. Allen, and Y. L. Yung (2005), Atmosphere of
747 Callisto, *J. Geophys. Res.*, *110*, E02003, 10.1029/2004JE002322.
748 Liang, M.-C., H. Hartman, R. E. Kopp, J. L. Kirschvink, and Y. L. Yung (2006), Production
749 of hydrogen peroxide in the atmosphere of a Snowball Earth and the origin of oxygenic
750 photosynthesis, *PNAS, 103*, 18896-18899.
751 Loeffler, M. J., U. Raut, R. A. Vidal, R. A. Baragiola, and R. W. Carlson (2006a), Synthesis
752 of hydrogen peroxide in water ice by ion irradiation, *Icarus*, *180*, 265-273.
753 Loeffler, M. J., U. Raut, and R. A. Baragiola (2006b), Enceladus: A source of nitrogen and an
754 explanation for the water, *Astrophys. J.*, *649*, L133-L136.
755 Matson, D. L., J. C. Castillo, J. Lunine, and T. V. Johnson (2007), Enceladus' plume:
756 Compositional evidence for a hot interior, *Icarus*, *187*, 569-573.
757 Maurice, S., E. C. Sittler, J. F. Cooper, B. H. Mauk, M. Blanc, and R. S. Selenick (1996),
758 Comprehensive analysis of electron observations at Saturn: Voyager 1 and 2, *J. Geophys.*
759 *Res.*, *101*, 15211-15232.
760 McCord, T. B., et al. (1998a), Salts on Europa's surface detected by Galileo's Near Infrared
761 Mapping Spectrometer, *Science*, *280*, 1242-1245.
762 McCord, T. B., et al. (1998b), Non-water-ice constituents in the surface material of the icy
763 Galilean satellites from the Galileo near-infrared mapping spectrometer investigation, *J.*
764 *Geophys. Res.*, *103*, 8603-8626.
765 McKinnon, W. B. (2006), On convection in ice I shells of outer Solar System bodies, with
766 detailed application to Callisto, *Icarus*, *183*, 435-450.
767 McKinnon, W. B., and A. C. Barr (2006), Structure and evolution of ice dwarf planets, *Bull.*
768 *Amer. Astron. Soc.*, *38*, 518.
769 Moore, M. H., and R. L. Hudson (2000), IR detection of H_2O_2 at 80 K in ion-irradiated
770 laboratory ices relevant to Europa, *Icarus*, *145*, 282-288.

771 Mumma, M. J., R. E. Novak, M. A. DiSanti, B. P. Bonev, and N. Dello Russo (2004),
772 Detection and mapping of methane and water on Mars, *Bull. Amer. Astron. Soc.*, *36*, 1127.
773 Newman, S. F., B. J. Buratti, R. H. Brown, R. Jaumann, J. Bauer, and T. Momary (2007),
774 The search for hydrogen peroxide on Enceladus, Lunar and Planetary Institute Conference
775 Abstracts, *38*, 1769.
776 Niemann, H. B., et al. (2005), The abundances of constituents of Titan's atmosphere from the
777 GCMS instrument on the Huygens probe, *Nature*, *438*, 779-784.
778 Nimmo, F., and R. T. Pappalardo (2006), Diapir-induced reorientation of Saturn's moon
779 Enceladus, *Nature, 441*, 614-616.
780 Noll, K. S., R. E. Johnson, A. L. Lane, D. L. Domingue, and H. L. Weaver (1996), Detection
781 of ozone on Ganymede, *Science*, *273*, 341-343.
782 Noll, K. S., T. L. Roush, D. P. Cruikshank, R. E. Johnson, and Y. J. Pendleton (1997),
783 Detection of ozone on Saturn's satellites Rhea and Dione, *Nature*, *388*, 45-47.
784 Owen, T. C. (2000), On the origin of Titan's atmosphere, *Plan. Sp. Sci., 48*, 747-752.
785 Pappalardo, R. T., et al. (1999), Does Europa have a subsurface ocean? Evaluation of the
786 geological evidence, *J. Geophys. Res.*, *104*, 24015-24055.
787 Paranicas, C., R. B. Decker, B. H. Mauk, S. M. Krimigis, T. P. Armstrong, and S. Jurac
788 (2004), Energetic ion composotion in Saturn's magnetosphere revisited, *Geophys. Res.*
789 *Lett.*, *31*, L04810, doi:10.1029/2003GL018899.
790 Phillips, C. B., A. S. McEwen, G. V. Hoppa, S. A. Fagents, R. Greeley, J. E. Klemaszewski,
791 R. T. Pappalardo, K. P. Klaasen, and H. H. Breneman (2000), The search for current
792 geologic activity on Europa, *J. Geophys. Res.*, *105*, 22579-22597.
793 Porco, C. C., et al. (2006), Cassini observes the active south pole of Enceladus, *Science*, *311*,
794 1393-1401.

795 Sagan, C. (1994), *Pale Blue Dot: A Vision of the Human Future in Space*, 1st edition, ISBN
796 0-679-43841-6, Random House, New York.

797 Schulze-Makuch, D., and J. M. Houtkooper (2006), Life on Mars? Reinterpretation of the
798 Viking life detection experiments: A possible biogenic origin of hydrogen peroxide, *Amer.*
799 *Astron. Soc. Meeting Abstracts*, *209*, 35.03.

800 Sittler, E. C., J. D. Scudder, and H. S. Bridge (1981), Distribution of neutral gas and dust near
801 Saturn, *Nature*, *292*, 711-714.

802 Sittler, E. C., Jr., et al. (2005), Preliminary results on Saturn's inner plasmasphere as observed
803 by Cassini: Comparison with Voyager, *Geophys. Res. Lett.*, *32*, L14S07,
804 doi:10.1029/2005GL022653.

805 Sittler, E. C., Jr., et al. (2006), Energetic nitrogen atoms within the inner magnetosphere of
806 Saturn, *J. Geophys. Res.*, *111*, A09223, doi:10.1029/2004JA010509.

807 Smith, H. T., M. Shappirio, E. C. Sittler, D. Reisenfeld, R. E. Johnson, R. A. Baragiola, F. J.
808 Crary, D. J. McComas, and D. T. Young (2005), Discovery of nitrogen in Saturn's inner
809 magnetosphere, *Geophys. Res. Lett.*, *32*, L14S03, 10.1029/2005GL022654.

810 Smith, H. T., R. E. Johnson, E. C. Sittler, M. Shappirio, D. Reisenfeld, O. J. Tucker, M.
811 Burger, F. J. Crary, D. J. McComas, and D. T. Young (2007), Enceladus: The likely
812 dominant nitrogen source in Saturn's magnetosphere, *Icarus*, *88*, 356-366.

813 Soderblom, L. A., T. L. Becker, S. W. Kieffer, R. H. Brown, C. J. Hansen, and T. V. Johnson
814 (1990), Triton's geyser-like plumes: Discovery and basic characterization, *Science*, *250*,
815 410-415.

816 Spahn, F., et al. (2006), Cassini dust measurements at Enceladus and implications for the
817 origin of the E ring, *Science*, *311*, 1416-1418.

818 Spencer, J. R., W. M. Calvin, and M. J. Person (1995), Charged-coupled device spectra of the
819 Galilean satellites: molecular oxygen on Ganymede, *J. Geophys. Res.*, *100*, 19049-19056.

820 Spencer, J. R., and W. M. Calvin (2002), Condensed O_2 on Europa and Callisto, *Astron. J.*,
821 *124*, 3400-3403.
822 Strobel, D. F., J. Saur, P. D. Feldman, and M. A. McGrath, Hubble Space Telescope Space
823 Telescope Imaging Spectrograph search for an atmosphere on Callisto: A jovian unipolar
824 inductor (2002), *Astrophys. J.*, *581*, L51-L54.
825 Spencer, J. R., J. C. Pearl, M. Segura, F. M. Flasar, A. Mamoutkine, P. Romani, B. J.
826 Buratti, A. R. Hendrix, L. J. Spilker, and R. M. C. Lopes (2006), Cassini encounters
827 Enceladus: Background and the discovery of a south polar hot spot, *Science, 311*, 1401–
828 1405.
829 Sturner, S. J., et al. (2003), Monte Carlo simulations and generation of the SPI response,
830 *Astron. Astrophys.*, *411*, L81-L84.
831 Tokar, R. L., et al. (2006). The interaction of the atmosphere of Enceladus with Saturn's
832 plasma, *Science*, *311*, 1409-1412.
833 Verbiscer, A., R. French, M. Showalter, and P. Helfenstein (2007), Enceladus: Cosmic
834 graffiti artist caught in the act, *Science*, *315*, 815.
835 Waite, J. H., et al. (2006), Cassini Ion and Neutral Mass Spectrometer: Enceladus plume
836 composition and structure, *Science*, *311*, 1419-1422.
837 Williams, D. J., R. W. McEntire, S. Jaskulek, and B. Wilken (1992), The Galileo Energetic
838 Particles Detector, *Sp. Sci. Rev.*, *60*, 385–412.
839 Ziegler, J. F., J. P. Biersack, and U. Littmark (1985), *The Stopping and Range of Ions in*
840 *Solids*, Pergamon Press, New York.
841
842 **Acknowledgements.** This work was supported in part by the Cassini Plasma Spectrometer
843 (CAPS) Project and the Space Physics Data Facility at Goddard Space Flight Center.

844

844

Table 1. Radiolytic Cryovolcanism Model Parameters for Enceladus

Body – Model	Particle Energy Flux mWm^{-2}	H_2O_2 Number Flux* $(cm^2\text{-}s)^{-1}$	Chemical Heat Flux mWm^{-2}	N_2 Source Flow $kg\ s^{-1}$	Plume Fluid Flow $kg\ s^{-1}$
Europa – e	100	$1.7x10^{11}$	5.4	3.8	3000
Enc – high e	2.1	$3.6x10^{9}$	0.11	0.08	64
Enc – mid e	0.7	$1.2x10^{9}$	0.039	0.027	22
Enc – low e	0.1	$1.7x10^{8}$	0.0054	0.0038	3.0
Enc – CRP	0.002	$3.4x10^{6}$	0.00011	$7.7x10^{-5}$	0.062
Rings – CRP	0.0005	$8.5x10^{5}$	$2.7x10^{-5}$	$1.9x10^{-5}$	0.015
40AU SolMin - CRP	0.003	$5.2x10^{6}$	0.00016	0.00012	0.096
HS – CRP	0.0035	$6.0x10^{6}$	0.00019	0.00013	0.10
LISM – CRP	0.0083	$1.4x10^{7}$	0.00044	0.00032	0.26

845 *Computed at maximum radiolytic yield G = 0.4 for H_2O_2.

846 Abbeviations: Enc – X – e (high, middle, and low electron flux models for Enceladus), CRP (cosmic ray
847 proton), Ring (Saturn's main rings), SolMin (solar minimum), HS (heliosheath), LISM (local interstellar
848 medium).

849

850

851

851 **Figure Captions**

852 **Figure 1.** Illustration of radiolytic gas-driven cryovolvanism for potential subsurface liquid
853 water reservoir near the surface of Enceladus. A continuous rain of energetic electrons
854 (yellow arrows) drives radiolysis and saturates the upper ice surface with oxidants (blue),
855 mostly H_2O_2 but with mix of other species. Transient plume activity ejects ice grains falling
856 back to the surface (white ballistic curves) and depositing multiple layers of water frost
857 (white) interspersed with oxidant concentrations accumulating during lower plume activity.
858 Ice upwelling continuously supplies fresh "fuels" (red), e.g. hydrates of CH_4 and NH_4, from
859 the deep interior. Exposure to increasing temperature within the ice margins of the fluid
860 reservoir initiates sequences of exothermic reactions from H_2O_2 dissociation to fuel
861 oxidation, resultant gas production, and fluid reservoir heating. Percolation of expanding hot
862 gas bubbles from the margins into the incompressible water fluid becomes the driving force
863 for upward movement (white arrows) of gas-saturated fluid to form the plumes. Interactions
864 of lower (left side) or higher (right side) concentrations of oxidants and fuels produce
865 correspondingly less or more gas.

866 **Figure 2.** Representative differential flux spectra of Saturn magnetospheric electrons at the
867 equatorial jovicentric orbits of the icy moons Mimas, Enceladus, Tethys, Dione, and Rhea as
868 determined from the SATRAD model [*Garrett et al.*, 2005].

869 **Figure 3.** Differential flux spectra of energetic electrons (red curves) at Enceladus and
870 Europa, respectively from the planetary magnetospheres of Saturn and Jupiter, and of cosmic
871 ray protons (black curves) irradiating icy bodies within and beyond the heliosphere. The
872 thickest solid Enceladus curve is from the SATRAD model. The two medium-thickness
873 Enceladus curves are respectively upper and lower limits from Voyager and Cassini/MIMI
874 electron data. The upper limit comes from Voyager measurements compiled by *Maurice et*
875 *al.* [1996], and the lower limit is from Cassini electron flux measurements by the
876 Magnetospheric Imaging Instrument (MIMI) experiment [*Krimigis et al.*, 2004] near the

877 Jupiter-fixed longitude of this moon during the 9 March 2005 flyby. The limiting flux curves
878 for Enceladus are extrapolated into the SATRAD curve at higher energies. The thinnest red
879 curves are MIMI measurements for other selected periods of Enceladus orbit crossings: Julian
880 days 48, 195, and 266 of 2005. A small peak at 0.03 MeV in the spectrum from day 48 is
881 from a transient injection event. The Europa flux spectrum [*Cooper et al.*, 2001] is a
882 composite of Galileo Orbiter data below 1 MeV from the Energetic Particle Detector
883 [*Williams et al.*, 1992] and Pioneer-Voyager model data [*Divine and Garrett*, 1983] at higher
884 energies up to 40 MeV. The Enceladus and Europa model spectra are extrapolated for surface
885 interaction modelling as power laws to 1000 MeV from the lower energy measurements.
886 Proton flux spectra are also shown as derived for cosmic ray protons (four dashed curves) in
887 the outer supersonic heliosphere within the classical Kuiper Belt near 40 AU and in the outer
888 heliospheric boundary regions [*Cooper et al.*, 2006] of the heliosheath and the local
889 interstellar medium. The two 40-AU spectra are respectively for minimum [*Cooper et al.*,
890 2003] and maximum solar activity, the latter data being provided from previously
891 unpublished Voyager data of co-author M. E. Hill.

892 **Figure 4.** Surface depth profiles in H_2O ice for time in years to accumulate chemically
893 significant dosages of 60 gigarad (~ 110 eV per irradiated H_2O molecule) from total
894 magnetospheric electron irradiation of Enceladus and Europa as compared to trans-neptunian
895 objects. The two thin solid curves show the partial contributions of higher energy electrons at
896 1–10 MeV and 10–100 MeV to the Enceladus total irradiation at 10 keV to 1000 MeV, as
897 compared to the total irradiation profile for Europa (dot-dot-dash curve). Comparative
898 profiles (dashed curves) are also shown for cosmic ray proton irradiation of objects near 40
899 AU near solar minimum [*Cooper et al.*, 2003] and on highly eccentric orbits [*Cooper et al.*,
900 2006] passing through the heliosheath and into the local interstellar medium. Dosage time
901 profiles are computed for isotropically incident fluxes onto flat surfaces from the flux spectra
902 in Figure 3. The GEANT radiation transport code (http://wwwasd.web.cern.ch/
903 wwwasd/geant/), as implemented in our earlier work [*Sturner et al.*, 2003; *Cooper et al.*,
904 2006], is used here for complete interactions of primary electrons, protons, and secondary

905 interaction products at energies above 10 keV from the flux spectra in Figure 3. Due to
906 limitations on spatial step resolution in GEANT, the proton profiles have been extended to
907 lower energies with stopping range and differential energy loss data of the Stopping and
908 Range of Ions in Matter (SRIM) model [*Ziegler et al.*, 1985] (http://www.srim.org/) also used
909 in the earlier work [*Cooper et al.*, 2001].
910
911

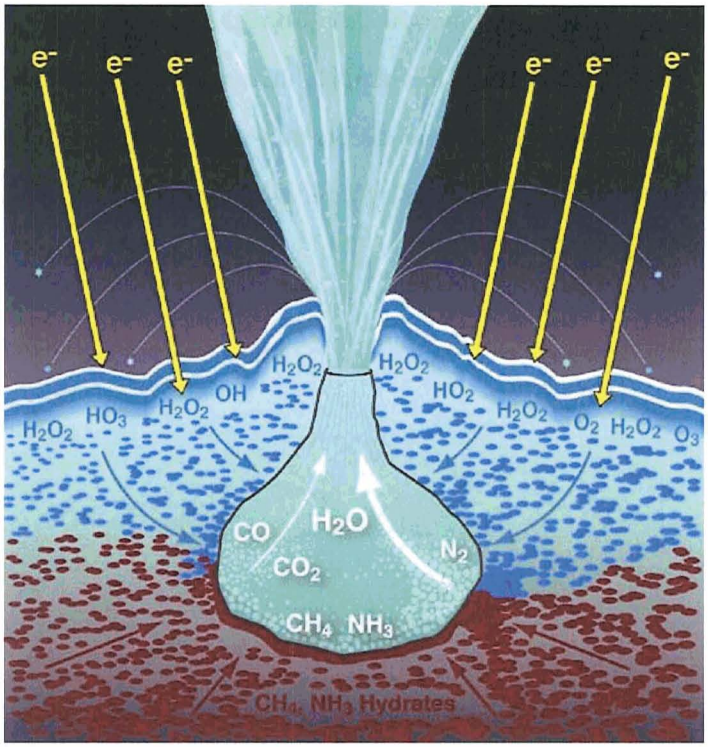

911

912 **Figure 1.** Illustration of radiolytic gas-driven cryovolvanism for potential subsurface liquid
913 water reservoir near the surface of Enceladus. A continuous rain of energetic electrons
914 (yellow arrows) drives radiolysis and saturates the upper ice surface with oxidants (blue),
915 mostly H_2O_2 but with mix of other species. Transient plume activity ejects ice grains falling
916 back to the surface (white ballistic curves) and depositing multiple layers of water frost
917 (white) interspersed with oxidant concentrations accumulating during lower plume activity.
918 Ice upwelling continuously supplies fresh "fuels" (red), e.g. hydrates of CH_4 and NH_4, from
919 the deep interior. Exposure to increasing temperature within the ice margins of the fluid
920 reservoir initiates sequences of exothermic reactions from H_2O_2 dissociation to fuel
921 oxidation, resultant gas production, and fluid reservoir heating. Percolation of expanding hot
922 gas bubbles from the margins into the incompressible water fluid becomes the driving force
923 for upward movement (white arrows) of gas-saturated fluid to form the plumes. Interactions
924 of lower (left side) or higher (right side) concentrations of oxidants and fuels produce
925 correspondingly less or more gas.

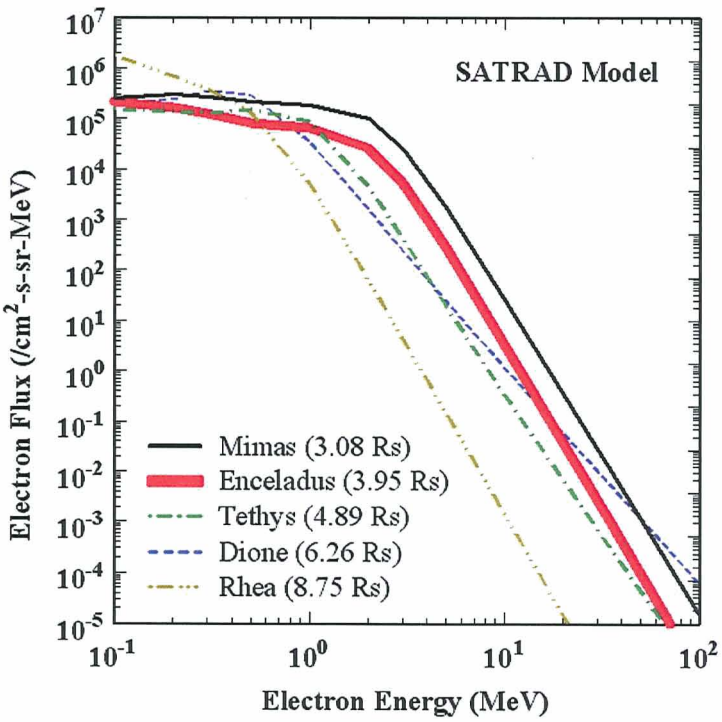

926

927 **Figure 2.** Representative differential flux spectra of Saturn magnetospheric electrons at the
928 equatorial jovicentric orbits of the icy moons Mimas, Enceladus, Tethys, Dione, and Rhea as
929 taken directly from the SATRAD model [*Garrett et al.*, 2005].

930

931

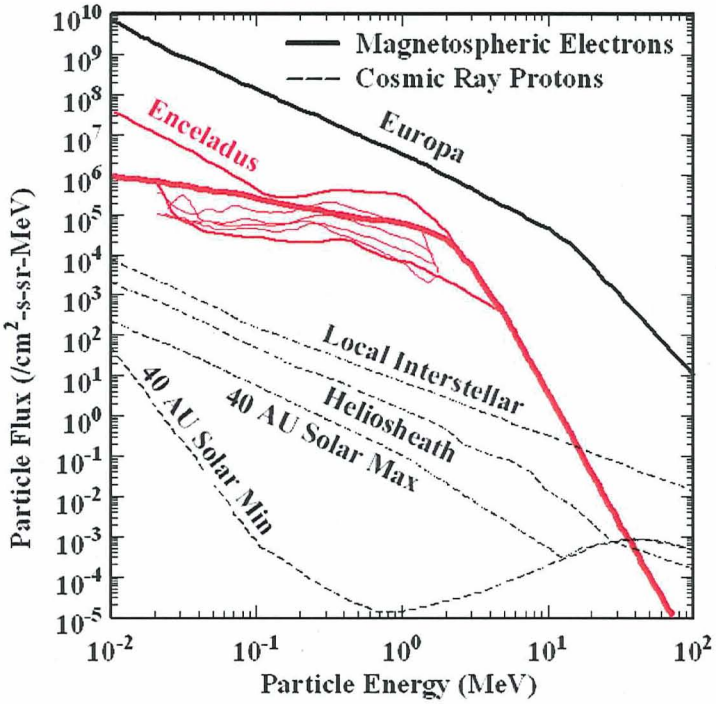

931

932 **Figure 3.** Differential flux spectra of energetic electrons (red curves) at Enceladus and
933 Europa, respectively from the planetary magnetospheres of Saturn and Jupiter, and of cosmic
934 ray protons (black curves) irradiating icy bodies within and beyond the heliosphere. The
935 thickest solid Enceladus curve is from the SATRAD model. The two medium-thickness
936 Enceladus curves are respectively upper and lower limits from Voyager and Cassini/MIMI
937 electron data. The upper limit comes from Voyager measurements compiled by *Maurice et*
938 *al.* [1996], and the lower limit is from Cassini electron flux measurements by the
939 Magnetospheric Imaging Instrument (MIMI) experiment [*Krimigis et al.*, 2004] near the
940 Jupiter-fixed longitude of this moon during the 9 March 2005 flyby. The limiting flux curves
941 for Enceladus are extrapolated into the SATRAD curve at higher energies. The thinnest red
942 curves are MIMI measurements for other selected periods of Enceladus orbit crossings: Julian
943 days 48, 195, and 266 of 2005. A small peak at 0.03 MeV in the spectrum from day 48 is
944 from a transient injection event. The Europa flux spectrum [*Cooper et al.*, 2001] is a
945 composite of Galileo Orbiter data below 1 MeV from the Energetic Particle Detector

946 [*Williams et al.*, 1992] and Pioneer-Voyager model data [*Divine and Garrett*, 1983] at higher
947 energies up to 40 MeV. The Enceladus and Europa model spectra are extrapolated for surface
948 interaction modelling as power laws to 1000 MeV from the lower energy measurements.
949 Proton flux spectra are also shown as derived for cosmic ray protons (four dashed curves) in
950 the outer supersonic heliosphere within the classical Kuiper Belt near 40 AU and in the outer
951 heliospheric boundary regions [*Cooper et al.*, 2006] of the heliosheath and the local
952 interstellar medium. The two 40-AU spectra are respectively for minimum [*Cooper et al.*,
953 2003] and maximum solar activity, the latter data being provided from previously
954 unpublished Voyager data of co-author M. E. Hill.
955
956

956

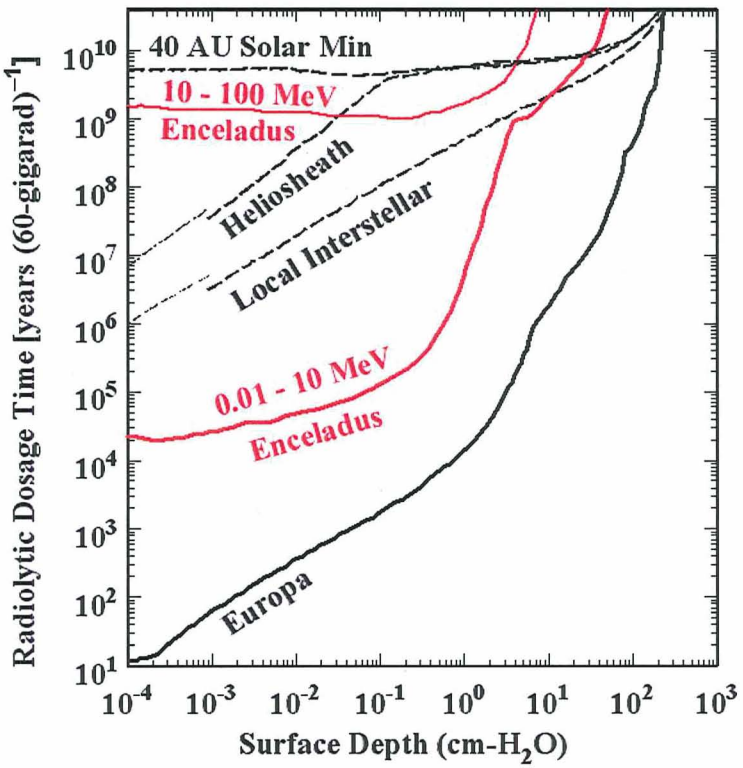

957

958 **Figure 4.** Surface depth profiles in H_2O ice for time in years to accumulate chemically
959 significant dosages of 60 gigarad (~ 110 eV per irradiated H_2O molecule) from total
960 magnetospheric electron irradiation of Enceladus and Europa as compared to trans-neptunian
961 objects. The two thin solid curves show the partial contributions of higher energy electrons at
962 1–10 MeV and 10–100 MeV to the Enceladus total irradiation at 10 keV to 1000 MeV, as
963 compared to the total irradiation profile for Europa (dot-dot-dash curve). Comparative
964 profiles (dashed curves) are also shown for cosmic ray proton irradiation of objects near 40
965 AU near solar minimum [*Cooper et al.*, 2003] and on highly eccentric orbits [*Cooper et al.*,
966 2006] passing through the heliosheath and into the local interstellar medium. Dosage time
967 profiles are computed for isotropically incident fluxes onto flat surfaces from the flux spectra
968 in Figure 3. The GEANT radiation transport code (http://wwwasd.web.cern.ch/
969 wwwasd/geant/), as implemented in our earlier work [*Sturner et al.*, 2003; *Cooper et al.*,

970 2006], is used here for complete interactions of primary electrons, protons, and secondary
971 interaction products at energies above 10 keV from the flux spectra in Figure 3. Due to
972 limitations on spatial step resolution in GEANT, the proton profiles have been extended to
973 lower energies with stopping range and differential energy loss data of the Stopping and
974 Range of Ions in Matter (SRIM) model [*Ziegler et al.*, 1985] (http://www.srim.org/) also used
975 in the earlier work [*Cooper et al.*, 2001].
976